

REMOVING RATE UNOBSERVABILITY IN SUN-HEADING FILTERS WITHOUT RATE GYROS

Thibaud Teil*, Hanspeter Schaub† and Scott Piggott‡

In a sun-heading determination scenario Coarse Sun-Sensors (CSS) can be paired with rate gyros in order to estimate sunline direction and rotation rate. These paired measurements allow for a fully observable sun-heading state vector. However, relying solely on CSS measurements for sun-heading and spacecraft rotation rate estimation is advantageous in scenarios where reliance on the fewest number of devices is desired. Here the challenge is to find a robust method for heading determination relying neither on rate gyros nor on spacecraft dynamics. In such a scenario, the rotation rate of the spacecraft is estimated in order to provide state derivative control or simply for better sun-heading estimation. Therefore, the state vector is traditionally the sun direction vector and its time derivative as seen by the body frame. A novel sun-heading filter is derived which estimates only the observable components of the body rate vector since the rate about the sun heading axis remains unobservable. By switching between kinematic formulations, it provides not only better sun-heading estimates, but also a partial body rate estimate. The new CSS filter provides the sun heading in a non-singular manner and estimates the observable component of the angular velocity vector. Both an extended Kalman filter formulation and a square-root unscented filter formulation are developed. The new filter is compared to two filters for gyro-less sun-heading estimation. One comparison filter uses a projection method to remove the unobservable rate component and another comparison filter uses numerical heading differences to estimate a rotation rate. The filters vary in state vectors, kinematics, and filter types, with the goal of controlling or removing non-observability. In order to compare the behavior of the set of sun-sensing algorithms, a modular filtering architecture is used and its utility is demonstrated. By incorporating this architecture in the Basilisk astrodynamics software package filter performances are compared through realistic scenarios.

INTRODUCTION

Coarse Sun-Sensors (CSSs) are small, relatively inexpensive, and regularly used for sunline heading determination. Cosine-type CSS devices output a voltage/current depending on the angle between the sensor normals and the sun direction. Although used in many micro and nano-satellite missions,^{1,2} they are also widely used in interplanetary missions including during safe-mode.³ More generally, heading determination provides target directions for the use of spacecraft pointing³ or to solve for attitude.⁴ As a 2-degree-of-freedom measurement, one heading does not provide full attitude or rate information on its own. Previous work has efficiently used both rate gyros and CSS

*Graduate Research Assistant, Aerospace Engineering Sciences, University of Colorado Boulder

†Glenn L. Murphy Chair of Engineering, Department of Aerospace Engineering Sciences, University of Colorado, 431 UCB, Colorado Center for Astrodynamics Research, Boulder, CO 80309-0431. AAS Fellow.

‡ADCS Integrated Simulation Software Lead, Laboratory for Atmospheric and Space Physics, University of Colorado Boulder.

measurements⁵ for efficient sun-heading determination, notably during periods of eclipse. The gyros help to forward integrate the sun-relative orientation until the spacecraft exits the eclipse. With enough CSSs—traditionally two pyramids of four with large fields of view—a spacecraft can always have at least one activated CSS, and frequently several activated devices. The resulting CSS data is sufficient for sun-heading determination during normal spacecraft operations. Outside of sun-heading estimation, gyros are often used successfully for attitude and body-rate determination^{6,7} while compensating for known or estimated drifts⁸ and biases.⁹

In contrast, some attitude determination modes use only of vector measurements¹⁰ or quaternions¹¹ without gyros. Other work focuses on single-gimbal moment Gyro control,¹² and attitude tracking with unknown gyro bias.¹³ Similarly, if the gyros are not sufficiently accurate, as might be the case with low-cost microelectromechanical systems rate gyros, this allows for a more robust sensor to determine attitude independently. Setting aside issues of observability, in a safe-mode scenario, it would also reduce the chances of using compromised measurements, and would reduce the additional sensors' associated power draw. Spacecraft dynamics properties have been used to observe the full rate vector¹⁴ through gyroscopic coupling. Yet, not using such dynamics also allows for minimalist and robust estimation. Mass properties change during the mission, particularly between trajectory correction maneuvers or insertion maneuvers. By being agnostic to mass properties and current actuator use one filter can provide sun-heading information throughout a mission. In a safe-mode context, the desire remains to use as little information as possible. If any actuators malfunction and their properties are hard-coded in the filter, its state estimation will be compromised as the filter dynamics will be incorrect.

In the absence of rate gyros, it is preferable to estimate rate, both for better states estimation and eventually for control. However, the desire to use CSS-only measurements for sun-heading determination exposes two observability issues. The first issue is that the spacecraft rotation vector's component about the sun-heading direction is unobservable. In order to use it more reliably in safe-mode, there needs to be progress made on this front: notably by decoupling the unobservable component from the states and eventually observing it through novel methods. Caution must be exercised regarding limited rate estimation using such measurements. Lessons learned from the LEWIS spacecraft^{15,16} show that unobservable rate components can build up without the attitude determination algorithm realizing it. If it is desirable to do full rate estimation using CSSs only, the dynamics must be added to couple the unobservable rate through Euler's equation.¹⁷ This does require the use of potentially changing dynamics in the filter, which is undesirable for a minimalist and robust formulation.

The second challenge is due to the fact that, depending on the CSS field of view, the problem can suffer from a more general lack of observability. Field of view designates the cone in which each individual sensor can be activated by incoming sunlight. This unobservability is due to the nature of CSS measurements,¹⁸ as they only provide angular information between the sensor normal and the sun-heading. This means that one CSS yields a cone of possibilities for the sun direction, two sensors lead to two possibilities, and only with three or more activated sensors do you get full observability instantaneously. If the sensors have a limited field of view, the spacecraft can go through time-spans with little information—not enough to determine the sun-heading uniquely.

Given these two challenges, this paper develops a novel kinematic formulation for sun-heading estimation. This formulation decouples the unobservable rate from the state vector. In previous works^{19,20} the spacecraft body rate relative to the inertial frame is not estimated by the filter. In order to do this, a frame switching paradigm is implemented in order to avoid singularities. This

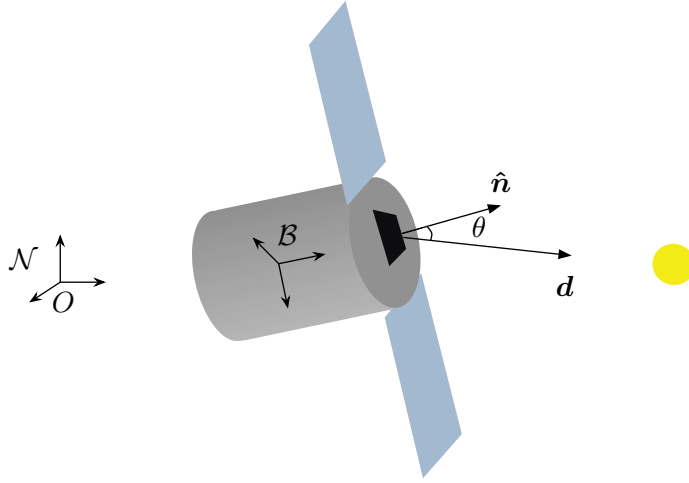


Figure 1. Spacecraft equipped with a CSS

implies rotating the states and covariance matrix when singularities are approached, and tracking the frames of interest.

Five filters are derived and their performances are compared. The first filter only estimates the sun-heading vector, and computes a partial solution to the satellite rotation rate at every step using the sun-heading estimates. The second and third subtract the unobservable components out of the states in an Extended Kalman Filter (EKF) and a square-root unscented Kalman Filter (SR-uKF) respectively. In the final formulation, the kinematics of the problem are reduced to a five-by-one vector estimating the sun direction and the observable rotation rate by tracking two different frames. This yields a minimal state vector with no unobservable states. By switching between two frames, the singularities can be avoided. As a novel derivation, it presents a promising approach to decoupling one of the observability problems in heading filters. This formulation is implemented in an EKF and a SR-UKF, and are referred to as Switch filters.

PROBLEM STATEMENT AND NOTATIONS

Scenario Description

This study analytically develops five two new sequential sun-heading and rate estimators and compares their performance to three other gyro-less filter implementations. To compare the filters, a scenario is created where a spacecraft is tumbling in deep space, and attempts to determine its sun-heading direction and rotation rate vector.

The sun-heading vector is estimated as a non-unit vector due to scale factors from the instruments.²¹ The sun-heading vector in the body frame is written ${}^B\mathbf{d}$, its inertial derivative is $\dot{\mathbf{d}}$, and its body frame derivative is \mathbf{d}' . The direction cosine matrix from an arbitrary \mathcal{S} frame into the spacecraft body frame \mathcal{B} will be $[\mathcal{BS}]$, and the inertial frame is labeled \mathcal{N} . The filtering notation used complies with Chapter 4 of Reference 22, and the dynamics notation complies with Reference 23.

Observability

One way to quantify the observability of a dynamical system is to compute the observability Grammian. The rank of this matrix determines the observability over a specified period of time: if it

Table 1. CSS Constellation

CSS Group	$\mathcal{B}_{\hat{n}_1}$	$\mathcal{B}_{\hat{n}_2}$	$\mathcal{B}_{\hat{n}_3}$	$\mathcal{B}_{\hat{n}_4}$
1	$\left[\frac{\sqrt{2}}{2}, -0.5, 0.5\right]^T$	$\left[\frac{\sqrt{2}}{2}, -0.5, -0.5\right]^T$	$\left[\frac{\sqrt{2}}{2}, 0.5, 0.5\right]^T$	$\left[\frac{\sqrt{2}}{2}, 0.5, -0.5\right]^T$
2	$\left[-\frac{\sqrt{2}}{2}, -0.5, 0.5\right]^T$	$\left[-\frac{\sqrt{2}}{2}, -0.5, -0.5\right]^T$	$\left[-\frac{\sqrt{2}}{2}, 0.5, -0.5\right]^T$	$\left[-\frac{\sqrt{2}}{2}, 0.5, 0.5\right]^T$

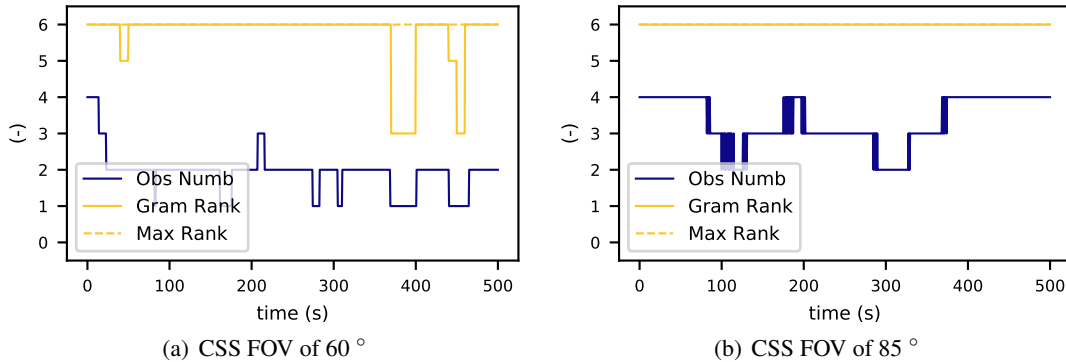


Figure 2. Rank of Observability Grammian and number of observations

is full rank, the system is observable, if not, there are unobservable states in the system. In a discrete-continuous context, the equation for the Observability Grammian is given in Equation (1). In this equation $[\Phi]$ represents the state transition matrix and $[H]_k$ represents the linearized measurement model evaluated at step k .

$$\forall (n, m) \in \mathbb{N}, m < n, \quad [G](t_m, t_n) = \sum_{t_k=t_m}^{t_n} [\Phi](t_k, t_m)^T [H]_k^T [H]_k [\Phi](t_k, t_m) \quad (1)$$

Throughout this paper, a double pyramid of four CSS devices each is used. The normals for each of the sensors are displayed in Table 1 this allows a maximal sensor coverage. The field of view of each of these sensors will dictate the number of sensors that are activated for a specific attitude.

Figure 2 shows simultaneously the number of activated sensors, and the observability Grammian defined in Equation (1). The term “field of view” is used to describe the half-angle to the cone of visibility for each individual sensor. In the case where the sun sensors have a half-angle field of view of 60° , seen in Figure 2(a), the Grammian is not always full rank. Because the rank value depends on the number of filter states, it is indicated with the yellow dotted line. For this plot, the sliding window used to compute the Grammian is of 10s, meaning $t_m - t_k = 10s$. Because the measurements are read at 2Hz, this sliding window used for the Grammian contains 20 measurements. This figure shows us that for a tumbling spacecraft there are several periods in which the states are not observable. This is corroborated by the coverage plot in Figure 3(a).

Nevertheless, fields of view can reach 85° with better quality sun-sensors and the results with this field of view can be seen in Figures 2(b), 3(b). This leads to a much higher number of activated sun-sensors at every instant, as seen in Figure 2. The observability Grammian is always full rank as the periods with only two activated CSS are brief, which is again corroborated by Figure 3(b).

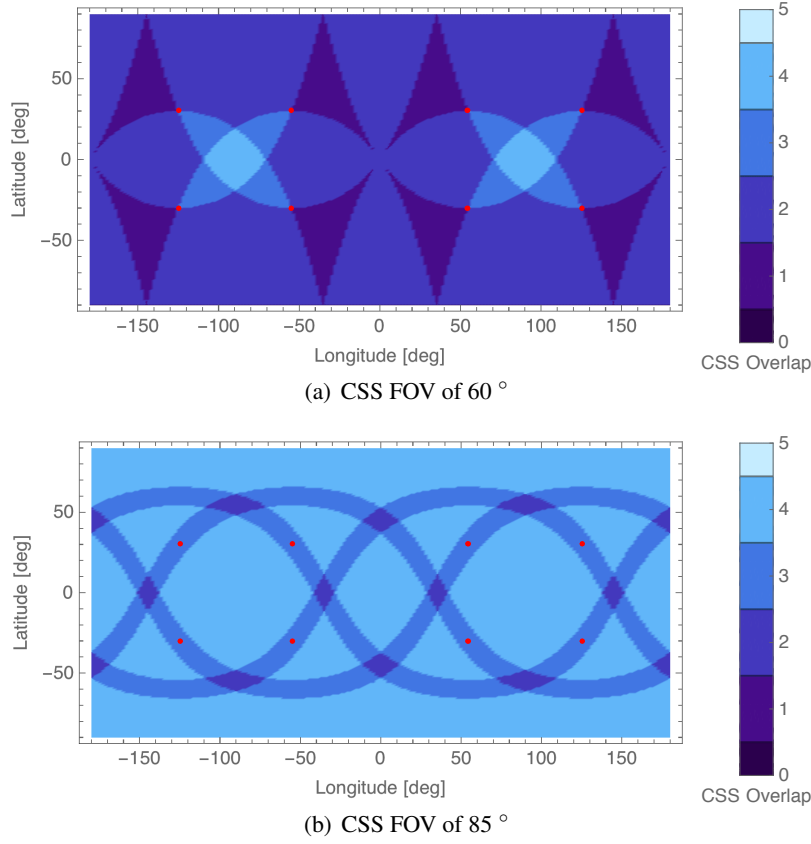


Figure 3. CSS coverage map illustrations. CSS headings are shown as red dots.

It is key to remember that this observability issue occurs in addition to the rate component being unobservable. There are therefore two issues: the sparsity of measurements at times which leads to a partially observable state, and a physically unobservable rate component along the sun-heading direction. Figures 2(a), 2(b) only speak to the former. The latter is the target of the kinematics derived in this work.

Measurements

The measurement model is given in Equation (2), and the linearized measurement model $[H]$ is defined as $[H] = \left[\frac{\partial G(\mathbf{X}, t_i)}{\partial \mathbf{X}} \right]^*$. In the following filters, the only measurements used are from the N CSS devices. For the i^{th} sensor, the measurement is simply given by the dot product of the sunline heading and the normal to the sensor:

$$G_i(\mathbf{X}) = \hat{\mathbf{n}}_i \cdot \mathbf{d} \quad (2)$$

This yields the partial derivatives for the $[H]$ matrix:

$$[H] = \begin{bmatrix} {}^B \hat{\mathbf{n}}_1^T & [0_{1 \times (n-3)}] \\ \vdots & \vdots \\ {}^B \hat{\mathbf{n}}_N^T & [0_{1 \times (n-3)}] \end{bmatrix} \quad (3)$$

where the rows contain the transposed normal vectors of the sensors that received measurements. The left-exponent notation indicates the frame with respect to which the vector components are taken. Hence the $[H]$ matrix has a changing size depending on the amount of measurements. Additionally the size of $[H]$ matrix depends on the number of states as seen in Equation (3).

FILTER KINEMATICS

Overview of Comparative Filters

There are many possible implementations of gyro-less sun-heading filters.²⁴ This subsection describes the formulations of previously implemented filters. This development sets up the mathematical frame work of CSS filters and illustrates the particular challenges of these solutions. The EKF algorithm used in these developments is explained and derived in Reference 22.

Sun-heading EKF The sun-heading EKF (‘Sun-EKF’ in following numerical simulations) is developed to use rate gyro measurements if they are available.¹⁸ In the case in which they are not, the rate is computed with the two previous sun-heading estimates. The state vector of this filter only contains the sunline vector in body frame components: $\mathbf{X} = {}^{\mathcal{B}}\mathbf{d}$. Given the nature of the filter, there is no unobservable state component as the inertial derivative of \mathbf{d} is not estimated.

The propagation equation is given in Equation (4), and is discretized using an Euler integration in Equation (5). This provides a simple and fast integration scheme. The tilde operator in Equation (4) is the matrix representation of the cross operator.

$$\mathbf{X}' = \mathbf{F}(\mathbf{X}) = {}^{\mathcal{B}}\mathbf{d}' = -[\tilde{\omega}_{\mathcal{B}/\mathcal{N}}]{}^{\mathcal{B}}\mathbf{d} \quad (4)$$

$${}^{\mathcal{B}}\mathbf{d}_{k+1} = {}^{\mathcal{B}}\mathbf{d}_k - \Delta t [\tilde{\omega}_{\mathcal{B}/\mathcal{N}}]{}^{\mathcal{B}}\mathbf{d}_k \quad (5)$$

Next the state dynamics matrix $[A]$ is found through:

$$[A] = \left[\frac{\partial \mathbf{F}(\mathbf{d}, t_i)}{\partial \mathbf{d}} \right] = -[\tilde{\omega}_{\mathcal{B}/\mathcal{N}}] \quad (6)$$

Gyro measurements are not being read by the filter but can be approximated^{19,20} by logging an extra time step of the sun-heading vector estimate \mathbf{d} .

$$\omega_k = \frac{1}{\Delta t} \frac{\mathbf{d}_k \times \mathbf{d}_{k-1}}{\|\mathbf{d}_k \times \mathbf{d}_{k-1}\|} \arccos \left(\frac{\mathbf{d}_k \cdot \mathbf{d}_{k-1}}{\|\mathbf{d}_k\| \|\mathbf{d}_{k-1}\|} \right) \quad (7)$$

Equation (7) uses the shorthand notation ω to signify $\omega_{\mathcal{B}/\mathcal{N}}$, and uses k as a time-step indice. Aliasing or noise issues are inherent to such a formulation. If the measurement times are too far apart with regard to the rate of change of the system, the rate may be poorly represented. On the other hand, if measurements are very close in time, the two vectors that are being crossed are nearly co-linear. This will lead to noise being amplified and an incorrect estimate of ω .

Subtracting unobservability The second filter derivation (called ‘EKF’ and ‘SR-uKF’ in the following numerical simulations) solves the rate unobservability by subtracting, from the state, the rate component along the sun-heading axis. The states that are estimated in this filter are the sunline vector, and its rate of change in the body frame $\mathbf{X} = \begin{bmatrix} {}^{\mathcal{B}}\mathbf{d} & {}^{\mathcal{B}}\mathbf{d}' \end{bmatrix}^T$.

The dynamics are given in Equation (8). Given the nature of the filter, the rotation about the \mathbf{d} axis remains unobservable. In order to remedy this, the states are projected along this axis and

subtracted, in order to measure only observable state components.

$$\mathbf{X}' = \mathbf{F}(\mathbf{X}) = \begin{bmatrix} \mathbf{F}_1(\mathbf{d}) \\ \mathbf{F}_2(\mathbf{d}') \end{bmatrix} = \begin{bmatrix} \mathbf{d}' - \left((\mathbf{d} \cdot \mathbf{d}') \frac{\mathbf{d}}{\|\mathbf{d}\|^2} \right) \\ -\frac{1}{\Delta t} \left((\mathbf{d} \cdot \mathbf{d}') \frac{\mathbf{d}}{\|\mathbf{d}\|^2} \right) \end{bmatrix} \quad (8)$$

Next the associated state dynamics matrix $[A]$ is found through:

$$[A] = \begin{bmatrix} \frac{\partial \mathbf{F}_1(\mathbf{X}, t_i)}{\partial \mathbf{d}} & \frac{\partial \mathbf{F}_1(\mathbf{X}, t_i)}{\partial \mathbf{d}'} \\ \frac{\partial \mathbf{F}_2(\mathbf{X}, t_i)}{\partial \mathbf{d}} & \frac{\partial \mathbf{F}_2(\mathbf{X}, t_i)}{\partial \mathbf{d}'} \end{bmatrix} = \begin{bmatrix} -\left(\frac{\mathbf{d}' \mathbf{d}^T}{\|\mathbf{d}\|^2} + (\mathbf{d} \cdot \mathbf{d}') \frac{\|\mathbf{d}\|^2 I - 2\mathbf{d}\mathbf{d}^T}{\|\mathbf{d}\|^4} \right) & I - \frac{\mathbf{d}\mathbf{d}^T}{\|\mathbf{d}\|^2} \\ -\frac{1}{\Delta t} \left(\frac{\mathbf{d}' \mathbf{d}^T}{\|\mathbf{d}\|^2} + (\mathbf{d} \cdot \mathbf{d}') \frac{\|\mathbf{d}\|^2 I - 2\mathbf{d}\mathbf{d}^T}{\|\mathbf{d}\|^4} \right) & -\frac{1}{\Delta t} \frac{\mathbf{d}\mathbf{d}^T}{\|\mathbf{d}\|^2} \end{bmatrix} \quad (9)$$

In order to implement another type of filter for state-estimation comparison, a square-root uncentred Kalman Filter is implemented using the same formulation. The implementation of this filter is denoted as EKF or SR-uKF according to the algorithm used. The SR-uKF has no need for partial derivative calculation which simplifies the code development to implement seen in Equation (9), and is used routinely for attitude determination.²⁵ As shown in Reference 26 the uKF uses $\alpha = 0.02$ as a constant determining the spread of the sigma points. The prior knowledge of the probability distribution of the state is set with $\beta = 2$ (which is optimal for Gaussian distributions).

The challenge with this filter is that the algorithm creates sun-heading rate \mathbf{d}' estimates at first assuming it is fully observable, then uses a projection to force the unobservable velocity component to be zero. Of interest is a filter that directly addresses this partial observability, and see how this filter performs relative to these earlier filters.

SWITCHING FILTERS

This section derives the switch-filter formulation (labeled ‘Switch-EKF’ and ‘Switch-SRuKF’ in the numerical simulations). This novel kinematic formulation utilizes the ability to switch between two frames to avoid singularities of the heading vector parameterization.

Frame Definitions

The switching filter attempts to avoid subtracting any terms from the estimate rate vector, while still enforcing the unobservable rate component is zero. In order to do this, an appropriate sensor frame $\mathcal{S} : \{\hat{\mathbf{s}}_1, \hat{\mathbf{s}}_2, \hat{\mathbf{s}}_3\}$ must be defined as pictured in Figure 4.

In order to not track the rate component alongside the sunline direction, a frame is defined such that the sunline direction is one of the basis vectors. Without loss of generality the sun heading measurement direction \mathbf{d} is chosen to be the aligned with the first base vector $\hat{\mathbf{s}}_1$

$$\hat{\mathbf{s}}_1 = \frac{\mathbf{d}}{\|\mathbf{d}\|} \quad (10)$$

Thus the rate component about $\hat{\mathbf{s}}_1$ is unobservable. The second and third \mathcal{S} -frame base vector are arbitrary as any choice keeps the unobservable rate component along $\hat{\mathbf{s}}_1$. A simple choice is to define

$$\hat{\mathbf{s}}_2 = \frac{\hat{\mathbf{s}}_1 \times \hat{\mathbf{b}}_1}{|\hat{\mathbf{s}}_1 \times \hat{\mathbf{b}}_1|} \quad (11)$$

$$\hat{\mathbf{s}}_3 = \hat{\mathbf{s}}_1 \times \hat{\mathbf{s}}_2 \quad (12)$$

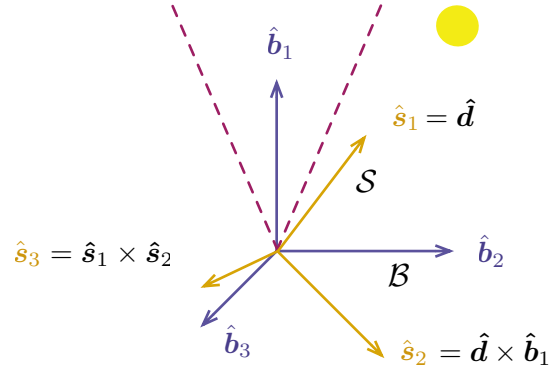


Figure 4. Frame built off the body frame for Switch filters

The problem that arises is the singularity that occurs when \hat{b}_1 and d are aligned as this switch frame \mathcal{S} is then undefined. To avoid this singularity an alternate sensor frame $\bar{\mathcal{S}}$ is defined which also has the first base vector aligned with the sun heading direction d . This approach is similar to how the QUEST attitude estimation algorithm²⁷ avoids a singularity by switching between two kinematic descriptions, or how the Modified Rodrigues Parameters switch between two alternate attitude representations.^{23,28} The underlying idea being that when approaching an ill-defined frame \mathcal{S} definition, a second frame $\bar{\mathcal{S}}$ is used. This frame $\bar{\mathcal{S}} = \{\hat{s}_1 = \hat{s}_1, \hat{s}_2, \hat{s}_3\}$ cannot be singular at the same time as \mathcal{S} : it uses the same first vector, but constructs \hat{s}_2 using \hat{b}_2 of the body frame. The last vector, once again, completes the orthonormal frame.

$$\hat{s}_2 = \frac{\hat{s}_1 \times \hat{b}_2}{|\hat{s}_1 \times \hat{b}_2|} \quad (13)$$

$$\hat{s}_3 = \hat{s}_1 \times \hat{s}_2 \quad (14)$$

By switching between the \mathcal{S} and $\bar{\mathcal{S}}$ frames the kinematic singularities are always avoided. The perpendicularity of \hat{b}_1 and \hat{b}_2 results in either \mathcal{S} or $\bar{\mathcal{S}}$ being nonsingular at all times. For example, whenever the sunline d gets within a cone of 30° of \hat{b}_1 , the frame is switched to $\bar{\mathcal{S}}$ which is not singular since the body vectors are orthonormal. Similarly, when d approaches \hat{b}_2 the frame is switched back to \mathcal{S} .

Because the two frames share the sunline vector d , both frames have the unobservable rate component along the first axis. Further, the sun heading to be estimate is the same first base vector. The vector components are mapped between the body frame \mathcal{B} and the two sensor frames \mathcal{S} and $\bar{\mathcal{S}}$ using the following Direction Cosine Matrices or DCMs:

$$[\mathcal{B}\mathcal{S}] = \begin{bmatrix} B_{\hat{s}_1} & B_{\hat{s}_2} & B_{\hat{s}_3} \end{bmatrix} \quad (15a)$$

$$[\mathcal{B}\bar{\mathcal{S}}] = \begin{bmatrix} B_{\hat{s}_1} & B_{\hat{s}_2} & B_{\hat{s}_3} \end{bmatrix} \quad (15b)$$

$$[\bar{\mathcal{S}}\mathcal{S}] = [\mathcal{B}\bar{\mathcal{S}}]^T [\mathcal{B}\mathcal{S}] \quad (15c)$$

Given a sun heading vector estimate d all these base vectors are know at any given time.

Filter Kinematics

The body rate relative to the inertial frame is projected onto the \mathcal{B} frame and the \mathcal{S} frame

$$\boldsymbol{\omega}_{\mathcal{B}/\mathcal{N}} = \omega_1 \hat{\mathbf{b}}_1 + \omega_2 \hat{\mathbf{b}}_2 + \omega_3 \hat{\mathbf{b}}_3 \quad (16)$$

$$= \omega_{s,1} \hat{\mathbf{s}}_1 + \omega_{s,2} \hat{\mathbf{s}}_2 + \omega_{s,3} \hat{\mathbf{s}}_3 \quad (17)$$

The rates of \mathcal{S} relative to the body and inertial frame are related as such: $\boldsymbol{\omega}_{\mathcal{S}/\mathcal{N}} - \boldsymbol{\omega}_{\mathcal{S}/\mathcal{B}} = \boldsymbol{\omega}_{\mathcal{B}/\mathcal{N}}$. The first vector of \mathcal{S} is the sun-heading which is considered to be constant in the inertial frame over the period of time required for heading determination. Hence, the only component of $\boldsymbol{\omega}_{\mathcal{S}/\mathcal{N}}$ that can vary is the rate about the sun-heading. Since the sunline rotation is impossible to extract from CSS measurements, the spacecraft is assumed to not be rotating about the sun-heading axis. This rate component is fundamentally unobservable and it is therefore set to zero.

In Equation (17), the previous assumption leads to $\omega_{s,1} = 0$. The body rate vector with the previous assumption is defined as follows:

$$\boldsymbol{\omega}^* = \boldsymbol{\omega}_{\mathcal{B}/\mathcal{N}}(\omega_{s,1} = 0) = \omega_{s,2} \hat{\mathbf{s}}_2 + \omega_{s,3} \hat{\mathbf{s}}_3 \quad (18)$$

$${}^{\mathcal{S}}\boldsymbol{\omega}^* = {}^{\mathcal{S}}[0 \quad \omega_{s,2} \quad \omega_{s,3}]^T \quad (19)$$

Zeroing this term prevents all motion of the \mathcal{S} frame relative to the inertial frame, hence the rate relationship becomes $-\boldsymbol{\omega}_{\mathcal{S}/\mathcal{B}} = \boldsymbol{\omega}^*$.

The filter state is therefore $\mathbf{X} = [{}^{\mathcal{B}}\mathbf{d} \quad \omega_{s,2} \quad \omega_{s,3}]^T$ and the kinematics are given by

$$\mathbf{X}' = \mathbf{F}(\mathbf{X}) = \begin{bmatrix} {}^{\mathcal{B}}\mathbf{d}' \\ \dot{\omega}_{s,2} \\ \dot{\omega}_{s,3} \end{bmatrix} = \begin{bmatrix} -{}^{\mathcal{B}}\boldsymbol{\omega}^* \times {}^{\mathcal{B}}\mathbf{d} \\ 0 \\ 0 \end{bmatrix} = \begin{bmatrix} {}^{\mathcal{S}} \begin{bmatrix} 0 \\ \omega_{s,2} \\ \omega_{s,3} \end{bmatrix} \times {}^{\mathcal{B}}\mathbf{d} \\ -[\mathcal{B}\mathcal{S}] \begin{bmatrix} 0 \\ \omega_{s,2} \\ \omega_{s,3} \end{bmatrix} \\ 0 \\ 0 \end{bmatrix} \quad (20)$$

$$[\mathbf{A}] = \left[\frac{\partial \mathbf{F}(\mathbf{d}, t_i)}{\partial \mathbf{X}} \right] = \begin{bmatrix} -[{}^{\mathcal{B}}\tilde{\boldsymbol{\omega}}^*] & -[\tilde{\mathbf{d}}] \begin{bmatrix} {}^{\mathcal{B}}\hat{\mathbf{s}}_2 & {}^{\mathcal{B}}\hat{\mathbf{s}}_3 \end{bmatrix} \\ [0]_{2 \times 3} & [0]_{2 \times 2} \end{bmatrix} \quad (21)$$

The 3×2 matrix in the dynamics matrix corresponds to the truncated DCM $[\mathcal{B}\mathcal{S}]$, and $\dot{\omega}$ is the time derivative of the scalar component ω .

This formulation leads to simple kinematics, much simpler than those of the filter which subtracts the unobservable states, yet can actually estimate the two observable vector components of the rate, instead of using past estimates of \mathbf{d} . In regard to the SR-uKF version of this filter, the same coefficients are used: $\alpha = 0.02$, and $\beta = 2$.

Switching Frames

The challenge that comes with the novelty of using two frames for the kinematics is switching between them. The new states $\bar{\mathbf{X}}$ and covariance $[\bar{P}]$ after the switch are

$$\bar{\mathbf{X}} = [\mathbf{W}]\mathbf{X} \quad [\bar{P}] = [\mathbf{W}][\mathbf{P}][\mathbf{W}]^T \quad (22)$$

Where \mathbf{X} and $[P]$ represent the state and covariance in the $\bar{\mathcal{S}}$ frame. The $[W]$ matrix maps the rate components from the \mathcal{S} frame to the $\bar{\mathcal{S}}$ frame when a switch occurs. The matrix $[W]$ is computed with

$$[W] = \begin{bmatrix} [I]_{3 \times 3} & [0]_{3 \times 2} \\ [0]_{2 \times 3} & \begin{bmatrix} \hat{\mathbf{s}}_2 \cdot \hat{\mathbf{s}}_2 & \hat{\mathbf{s}}_2 \cdot \hat{\mathbf{s}}_3 \\ \hat{\mathbf{s}}_3 \cdot \hat{\mathbf{s}}_2 & \hat{\mathbf{s}}_3 \cdot \hat{\mathbf{s}}_3 \end{bmatrix} \end{bmatrix} \quad (23)$$

using the previously computed \mathcal{S} and $\bar{\mathcal{S}}$ frame base vectors. The sun-heading vector \mathbf{d} is unmodified, while the rates are rotated into the switched frame. This equation assumes the switch is going from the \mathcal{S} frame to $\bar{\mathcal{S}}$ (the reciprocal is equivalent), and

$$\begin{bmatrix} \hat{\mathbf{s}}_2 \cdot \hat{\mathbf{s}}_2 & \hat{\mathbf{s}}_2 \cdot \hat{\mathbf{s}}_3 \\ \hat{\mathbf{s}}_3 \cdot \hat{\mathbf{s}}_2 & \hat{\mathbf{s}}_3 \cdot \hat{\mathbf{s}}_3 \end{bmatrix}$$

corresponds to the bottom left 2×2 submatrix of $[\bar{\mathcal{S}}\mathcal{S}]$. Equation (23) therefore provides a first order frame change for the covariance, allowing for the filter to continue its state estimation nominally.

Process Noise for Switch-EKF

Another nuance that arises when writing EKFs is the process noise formula. This is addressed by deriving the $[\Gamma]$ matrix that transports the noise to the state space given the new state vector. The time update of the error covariance matrix from time t_k to t_{k+1} ($\Delta t = t_{k+1} - t_k$) is given in Equation (24). The process noise matrix $[Q]$ is added via the $[\Gamma]$ matrix defined in Equation (25).²² Process noise is only added on the accelerations, meaning that $[B] = \begin{bmatrix} [0]_{3 \times 3} \\ [I]_{3 \times 3} \end{bmatrix}$ when there are 6 states.

$$[P]_{k+1} = [\Phi](t_{k+1}, t_k)[P]_k[\Phi](t_{k+1}, t_k)^T + [\Gamma](t_{k+1}, t_k)[Q][\Gamma](t_{k+1}, t_k)^T \quad (24)$$

$$[\Gamma](t_{k+1}, t_k) = \int_{t_k}^{t_{k+1}} [\Phi](t_{k+1}, \tau)[B](\tau)d\tau \quad (25)$$

In the earlier filters (the EKF and the SR-uKF), the second half of the state vector is a direct derivative of the sun-heading vector. Regarding state noise compensation, this allows the approximation in Equation (26), along with the fact that measurements are received frequently with regard to the evolution of the dynamics.

$$[\Gamma](t_{k+1}, t_k) = \Delta t \begin{bmatrix} \frac{\Delta t}{2}[I]_{3 \times 3} \\ [I]_{3 \times 3} \end{bmatrix} \quad (26)$$

This does not hold for the switch filter as $[\Phi]$ is a 5 by 5 matrix. In order to simplify the notation of partials in this section, $\bar{\omega}$ will represent the 2×1 matrix $[\omega_{s,2} \quad \omega_{s,3}]^T$

$$[\Phi](t_{k+1}, \tau) = \begin{bmatrix} [\Phi_1]_{3 \times 3} & [\Phi_2]_{3 \times 2} \\ [\Phi_3]_{2 \times 3} & [\Phi_4]_{2 \times 2} \end{bmatrix} = \begin{bmatrix} \frac{\partial \mathbf{d}(t_{k+1})}{\partial \mathbf{d}(\tau)} & \frac{\partial \mathbf{d}(t_{k+1})}{\partial \bar{\omega}(\tau)} \\ \frac{\partial \bar{\omega}(t_{k+1})}{\partial \mathbf{d}(\tau)} & \frac{\partial \bar{\omega}(t_{k+1})}{\partial \bar{\omega}(\tau)} \end{bmatrix} \quad (27)$$

Equation (27) uses the fact that $[\Phi](t_{k+1}, \tau) = \frac{\partial \mathbf{X}(t_{k+1})}{\partial \mathbf{X}(\tau)}$, and that $\mathbf{X} = [\mathbf{d} \quad \bar{\omega}]^T$. With this, Equation (26) can be re-written as Equation (28).

$$[\Gamma](t_{k+1}, t_k) = \int_{t_k}^{t_{k+1}} \begin{bmatrix} [\Phi_1]_{3 \times 3} & [\Phi_2]_{3 \times 2} \\ [\Phi_3]_{2 \times 3} & [\Phi_4]_{2 \times 2} \end{bmatrix} \begin{bmatrix} [0]_{3 \times 3} \\ [I]_{3 \times 3} \end{bmatrix} d\tau = \int_{t_k}^{t_{k+1}} \begin{bmatrix} [\Phi_2]_{3 \times 2} \\ [\Phi_4]_{2 \times 2} \end{bmatrix} d\tau \quad (28)$$

Table 2. Simulation Parameters

Parameter	$\boldsymbol{\sigma}(t_0)$	$\boldsymbol{\omega}(t_0)$ (°/s)	$[I]$ (kg/m ²)	Mass (kg)	simulation time (s)
Value	$[0, 0, 0]^T$	$[0.5, -0.5, -1]^T$	diag(900,800,600)	750	500

Table 3. Monte-Carlo Dispersions

Parameter	$\boldsymbol{\sigma}(t_0)$	$\boldsymbol{\omega}(t_0)$ (°/s)
Fast Distribution	$\mathcal{U}[0, 2\pi]$	$\pm\mathcal{N}[0.45, 0.55]$
Nominal Distribution	$\mathcal{U}[0, 2\pi]$	$\pm\mathcal{N}[0.05, 0.15]$
Slow Distribution	$\mathcal{U}[0, 2\pi]$	$\pm\mathcal{N}[0.001, 0.01]$

These submatrices of the state transition matrix now need to be approximated. As before, assuming dense tracking data, $[\Phi_4]_{2 \times 2} = \frac{\partial \tilde{\boldsymbol{\omega}}(t_{k+1})}{\partial \tilde{\boldsymbol{\omega}}(\tau)} \approx [I]_{2 \times 2}$. Then, by defining the $[J]$ matrix as

$$[J] = \begin{bmatrix} [0]_{1 \times 2} \\ [I]_{2 \times 2} \end{bmatrix} \quad (29)$$

The rate notations are reconciled through ${}^S\boldsymbol{\omega}^* = [J]\tilde{\boldsymbol{\omega}}$. Without specifying a frame, the propagation function yields

$$\mathbf{d}_{k+1} - \mathbf{d}_\tau = (t_{k+1} - \tau)[\tilde{\mathbf{d}}_\tau]\boldsymbol{\omega}^* \quad (30)$$

By then moving into the body frame,

$$\frac{\partial {}^B\mathbf{d}(t_{k+1})}{\partial \tilde{\boldsymbol{\omega}}(\tau)} = (t_{k+1} - \tau)[{}^B\tilde{\mathbf{d}}_\tau][\mathcal{BS}][J] \quad (31)$$

$$[\Phi_2]_{3 \times 2} = (t_{k+1} - \tau)[{}^B\tilde{\mathbf{d}}_\tau] \begin{bmatrix} {}^B\hat{\mathbf{s}}_2 & {}^B\hat{\mathbf{s}}_3 \end{bmatrix} \quad (32)$$

Therefore, assuming the state does not vary over the time between two updates, $[\Phi_2]_{3 \times 2}$ can be integrated to approximate $[\Gamma]$.

$$[\Gamma](t_{k+1}, t_k) = \int_{t_k}^{t_{k+1}} \begin{bmatrix} [\Phi_2]_{3 \times 2} \\ [\Phi_4]_{2 \times 2} \end{bmatrix} d\tau = \Delta t \begin{bmatrix} \frac{\Delta t}{2} [{}^B\tilde{\mathbf{d}}_k] \begin{bmatrix} {}^B\hat{\mathbf{s}}_2 & {}^B\hat{\mathbf{s}}_3 \end{bmatrix} \\ [I]_{2 \times 2} \end{bmatrix} \quad (33)$$

This leads to the new $[\Gamma]$ matrix in Equation (33), which is used for state noise compensation.

SIMULATION AND RESULTS

Five filters were developed out of the three kinematic formulations described in the previous section. The subtraction of the unobservable states formulation is written into a square-root unscented Kalman Filter (SR-uKF), and an Extended Kalman Filter (EKF). The formulation which only estimates the sunline direction is implemented in an EKF (Sunline-EKF). Finally the novel formulation is written in a EKF and SR-uKF (Switch-EKF, and Switch-SRuKF).

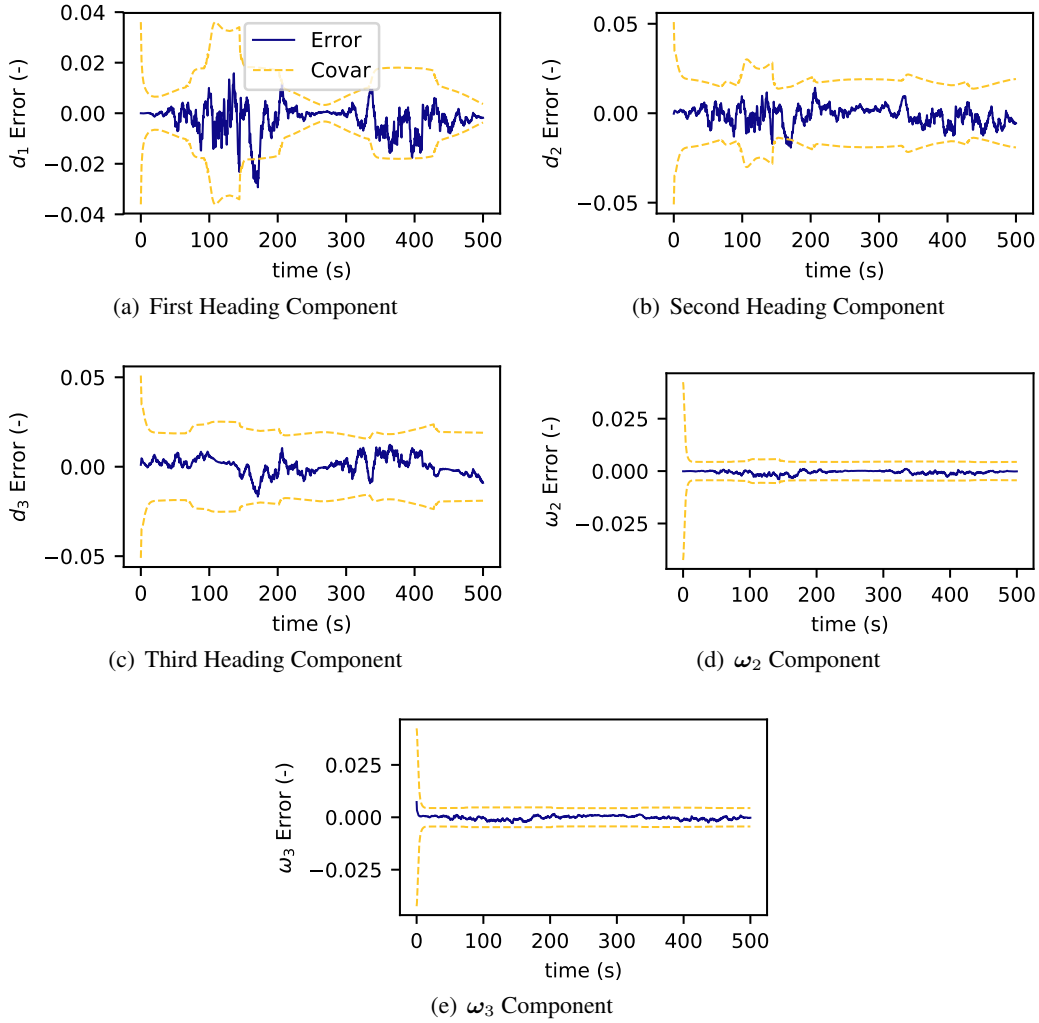


Figure 5. State Error and Covariance Plots of Switch-EKF, FOV: 85°

The simulation used is created using the Basilisk Software Package^{29*}. All runs simulate a tumbling spacecraft in deep space, at 1AU from the sun. The problem assumes that the time needed for control is much smaller than the time needed to orbit around the Sun, meaning that $\dot{\mathbf{d}} \approx \mathbf{0}$. The satellite is therefore not put on orbit around the Sun, but kept in a constant position in the inertial frame. The simulations inputs are listed in Table 2. This framework allows for a fully coupled dynamic simulation, and the runs use the same physical scenario (including noise), with only the filters changing between runs. The general simulation parameters used outside of Monte-Carlo analysis are summarized in Table 3.

For all of the results, the filters retain the same process noise which is listed in Table 4. These values are chosen by reducing the post-fit residuals to noise at slow spacecraft rotation rates which is the most common state for a controlled spacecraft. It is then desirable to test the robustness of these filters as such in order to determine which ones are the best overall.

*<http://hanspeterschaub.info/bskMain.html>

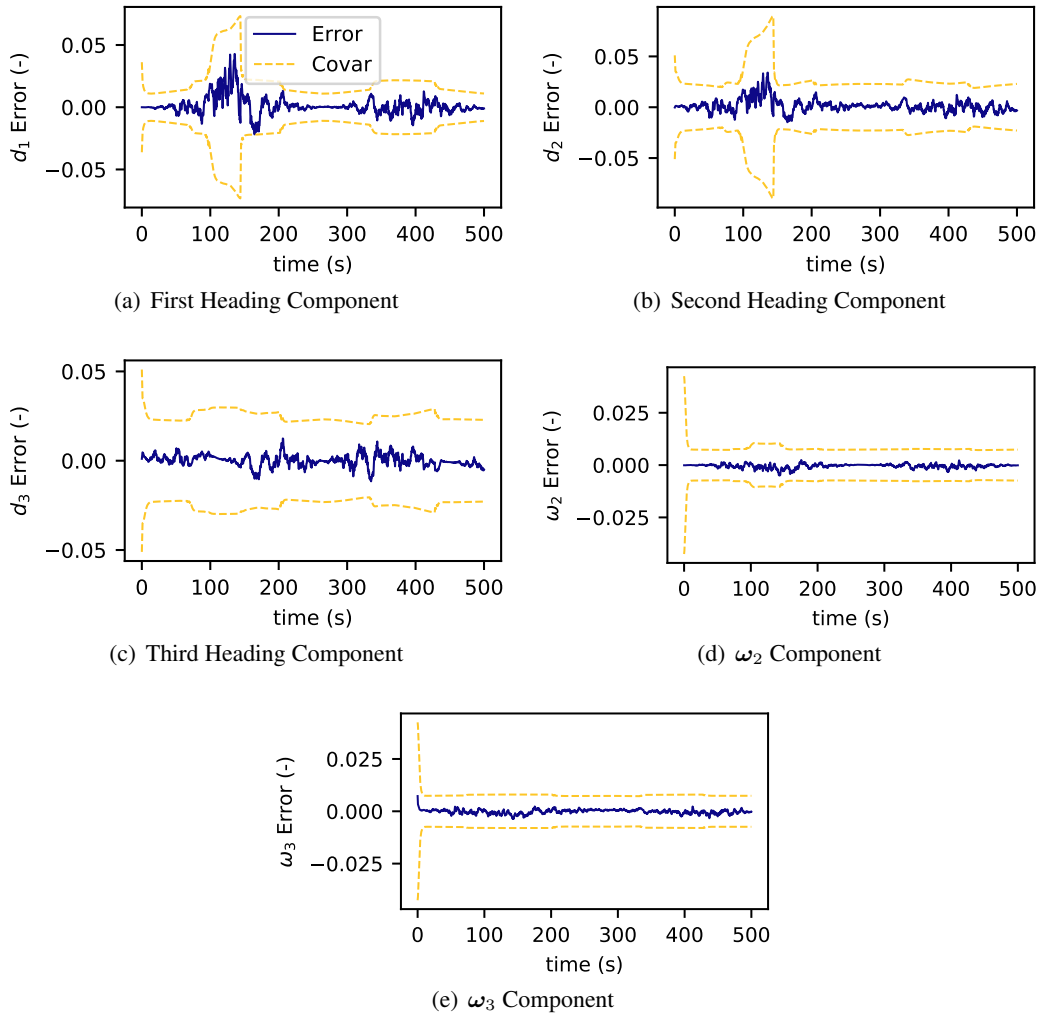


Figure 6. State Error and Covariance Plots of Switch-SRuKF, FOV: 85°

First the Switch filters are examined to ensure proper implementation and behavior. Second, all the implementations are compared in a scenario in order to observe overall performance and covariance behavior. Finally, the best filters are run in Monte-Carlo simulations with low and high observability to show the best overall performing filters.

Switch Filter Results

This subsection examines the implementation of the Switch-EKF and Switch-SRuKF. These results are created using the simulation parameters of Table 2, which initialize the spacecraft in a mild tumble. Figure 5 shows the state error and covariance for the Switch-EKF filter, while Figure 6 shows the Switch-SRuKF. Both these filters perform well as the state errors are within the covariance bounds and unbiased.

This is seen more specifically with the post-fit residuals seen in Figure 7 from the Switch-SRuKF run. The measurements are brought down to noise, with the expected standard deviations which is expected since the simulation doesn't have any un-modeled forces acting on the spacecraft. The

Table 4. State Noise Compensation (SNC)

Filter	Sunline-EKF	EKF	SR-uKF	Switch-EKF	Switch-uKF
SNC on d	10^{-2}	N/A	10^{-3}	N/A	10^{-3}
SNC on rates	N/A	$2 \cdot 10^{-4}$	$2 \cdot 10^{-4}$	$8 \cdot 10^{-4}$	$8 \cdot 10^{-4}$

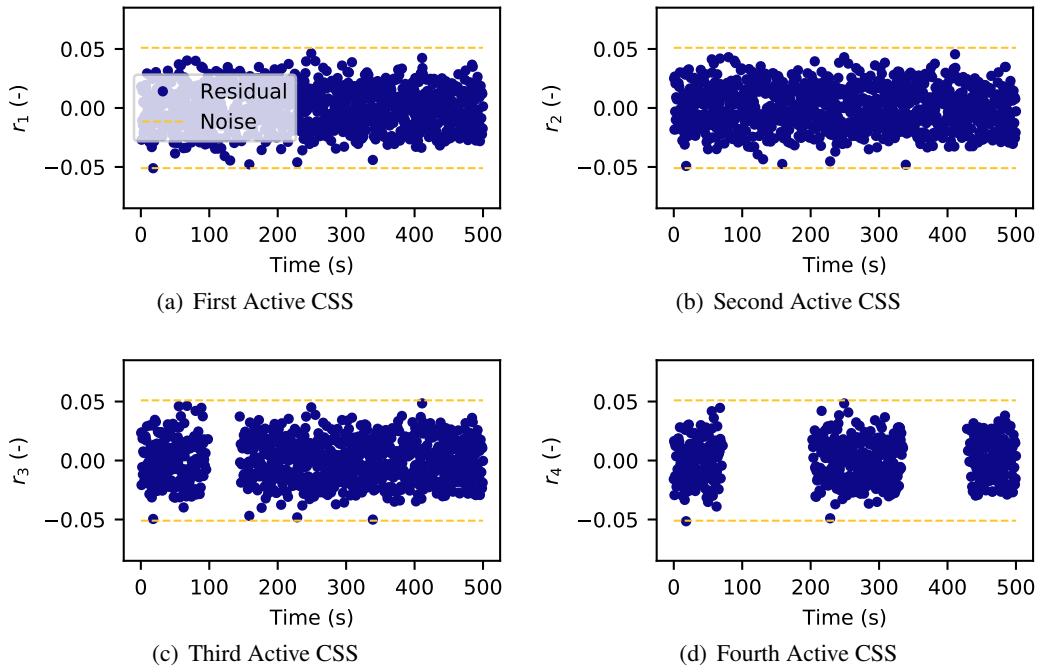


Figure 7. Post Fit Residuals for Switch-SRuKF, FOV: 85°

Table 5. Post Fit Residuals in nominal case, FOV: 85°

Filter	Statistics	Obs 1	Obs 2	Obs 3	Obs 4
Sunline-EKF	Means	-0.0007	0.0023	-0.009	0.0139
	Standard Deviations	0.0331	0.0313	0.0508	0.0351
EKF	Means	-0.0019	0.0004	0.0001	-0.0021
	Standard Deviations	0.0181	0.0198	0.0186	0.0182
SR-uKF	Means	0.0013	0.0027	0.0029	0.0096
	Standard Deviations	0.0187	0.0244	0.0344	0.0692
Switch-EKF	Means	-0.0026	-0.0004	0.0006	-0.0012
	Standard Deviations	0.0191	0.033	0.0356	0.0175
Switch-SRuKF	Means	0.0	0.001	0.0025	0.0096
	Standard Deviations	0.0186	0.0243	0.0343	0.0692

Switch-EKF post-fits are not displayed, but are nearly identical and provide confidence that the filter is working optimally.

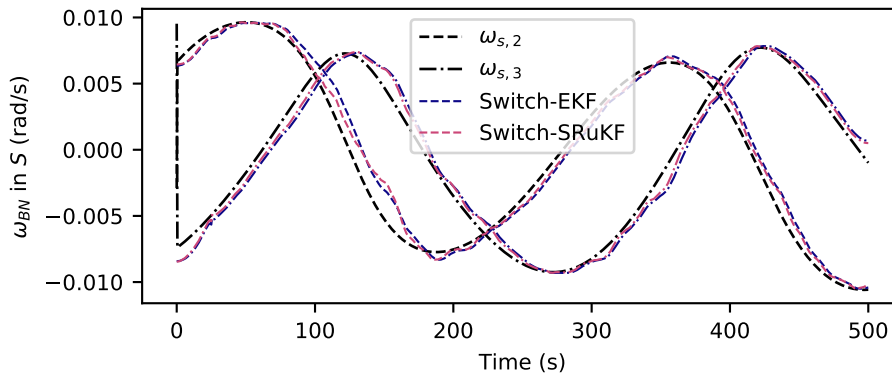
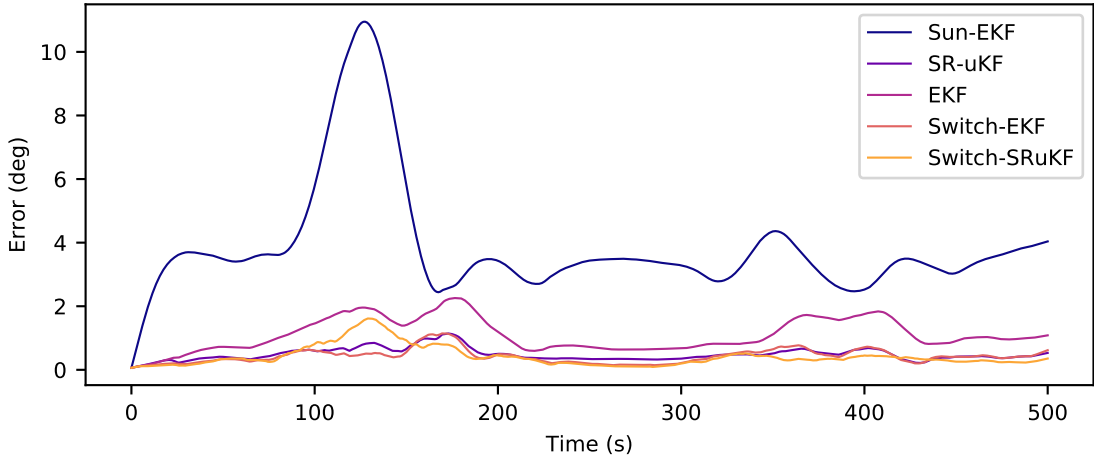


Figure 8. Switch Filters tracking the rates in the S frame

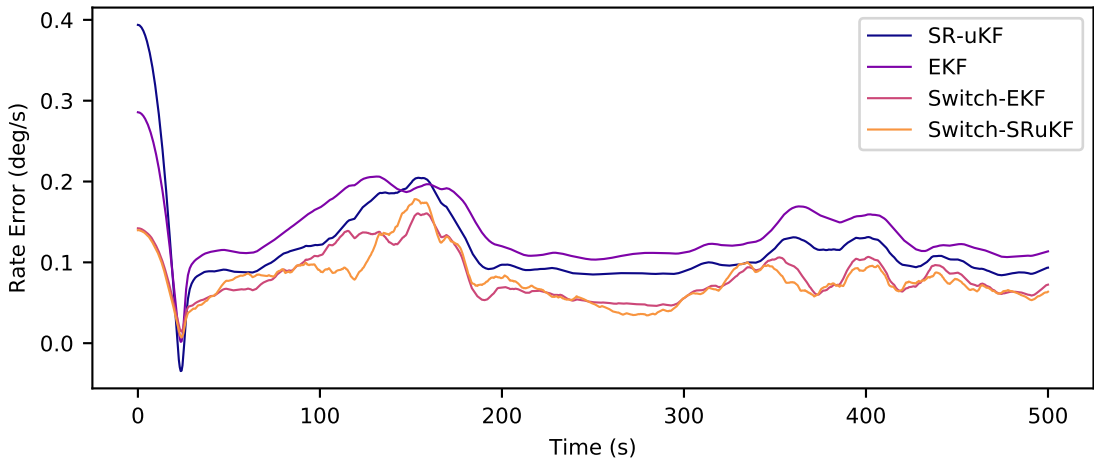
Figure 8 shows one of the novel components of the Switch filters: direct body rate estimation. The filters can be seen tracking the true body rates in the S frame (disregarding the unobservable component which is set to zero). Although just two components of this vector does not yet allow to fully estimate the body rate without extra information, it proves that the filters are functioning. Furthermore, if additional headings were tracked and fused full body rate estimation would be achievable.

General results

The simulation runs the filters with good and low quality measurements. As described previously, the filters are calibrated for their post-fit residuals to be noise at low speeds. With a field of view of 85° on each sensor, the problem has good observability, as seen in Figures 2(b), 3(b). Table 5 shows the post fit residuals' means and standard deviations for each of the activated devices. All



(a) Pointing Miss-Angle ($^{\circ}$)



(b) d' norm error

Figure 9. Comparative performance of the filters, FOV: 85°

the means are near zero which indicates no biases, while standard deviations are very close to the measurement noise of the instruments. These specific results are plotted in this section. The lower quality measurements (Figures 2(a), 3(a)) are studied as well in the Monte-Carlo subsection.

$$\dot{\mathbf{d}} = \mathbf{0} = \mathbf{d}' + \boldsymbol{\omega}_{\mathcal{B}\mathcal{N}} \times \mathbf{d} \quad (34)$$

These filters are compared by plotting their off-pointing in degrees and the norm of the error on \mathbf{d}' in Figures 9. For the switch filters (which do not estimate \mathbf{d}') the rate is mapped back using the transport theorem as seen in Equation (34). Knowledge of \mathbf{d} and \mathbf{d}' does not allow identification of the body rate uniquely due to the rank deficiency of the cross operator. Hence, the current estimate of the sun-heading and the observable components of the body rate are used to compute \mathbf{d}' . The data is smoothed using a Savitzky-Golay algorithm³⁰ in order to differentiate between the curves more easily. This algorithm does lead to a spike at the end of Figure 9(a) and Figure 9(b).

Figure 9(a) shows the off-pointing errors of all the filters and Figure 9(b) displays the rate error.

Table 6. RMS Errors from Truth, FOV: 85°

Filter	Sunline-EKF	EKF	SR-uKF	Switch-EKF	Switch-uKF
d RMS Pointing Error (°)	2.388	0.678	0.315	0.304	0.334
d' RMS Error (-)	N/A	0.089	0.087	0.055	0.056

Table 7. RMS Errors from Truth, FOV: 60°

Filter	Sunline-EKF	EKF	SR-uKF	Switch-EKF	Switch-SRuKF
d RMS Pointing Error (°)	7.651	4.695	3.003	3.568	2.151
d' RMS Error (-)	N/A	0.168	0.139	0.17	0.117

Tables 6 and 7 show the computed RMS errors for the filters in both the 85° and 60° FOV cases. The results show that the Switch filters outperforms the others both in rate and heading estimation. Due to the process noise on the body rates, the Switch filters sun-heading errors are slightly higher than some other results at low-speed tumbles. Yet at these speeds, all the filters provide errors that are less than half of a degree off. This can be seen more clearly in Figure 11(a).

Monte-Carlo analysis

In this subsection, the a Monte-Carlo analysis is run on the scenario. The dispersed parameters are the initial conditions to the spacecraft tumble: initial attitude and attitude rate. This general study allows one to ensure that the better performance of a specific filter is not attributed to favorable initial conditions. The dispersions are applied in 3 different scenarios. The first being a slowly rotating spacecraft scenario. This is the scenario to which all the filters are calibrated. The second scenario is a nominal rotation, akin to a slow maneuver. The third scenario is a fast rotation spacecraft similar to a tumble. The dispersions applied in each of these cases are listed in Table 3 in the Appendix.

Figure 10 shows the results of 10 Monte-Carlo runs in the high-observability scenario. For clarity, the Sunline-EKF filter—which was not performing as well as the others—is removed from this analysis. This allows for a more focused analysis on the best filters. These runs show that the Switch-uKF performs consistently better than its competitors. At slow speeds the difference between all the filters is hard to gauge since this is the run that calibrated the process noise. It does seem that despite overall excellent performance, this is the only realm where the Switch formulations do not estimate sun-heading better than the others. Yet the Switch formulations, and more notably the Switch-SRuKF, handle the faster spacecraft rates considerably better than the other filters.

Figure 11 shows the results of 10 Monte-Carlo runs in the low-observability scenario. The Monte-Carlos at low speeds also contain very low observability scenarios where no more than 2 or 3 sensors are activated, which yield high errors. With fewer measurements all the filters perform less well, yet once again the Switch-SRuKF consistently yields the smallest heading errors. This shows the value of this formulation: in the event of component failure, the Switch filters will provide consistently better sun-heading estimates. This contributes to the robustness of the attitude determination system.

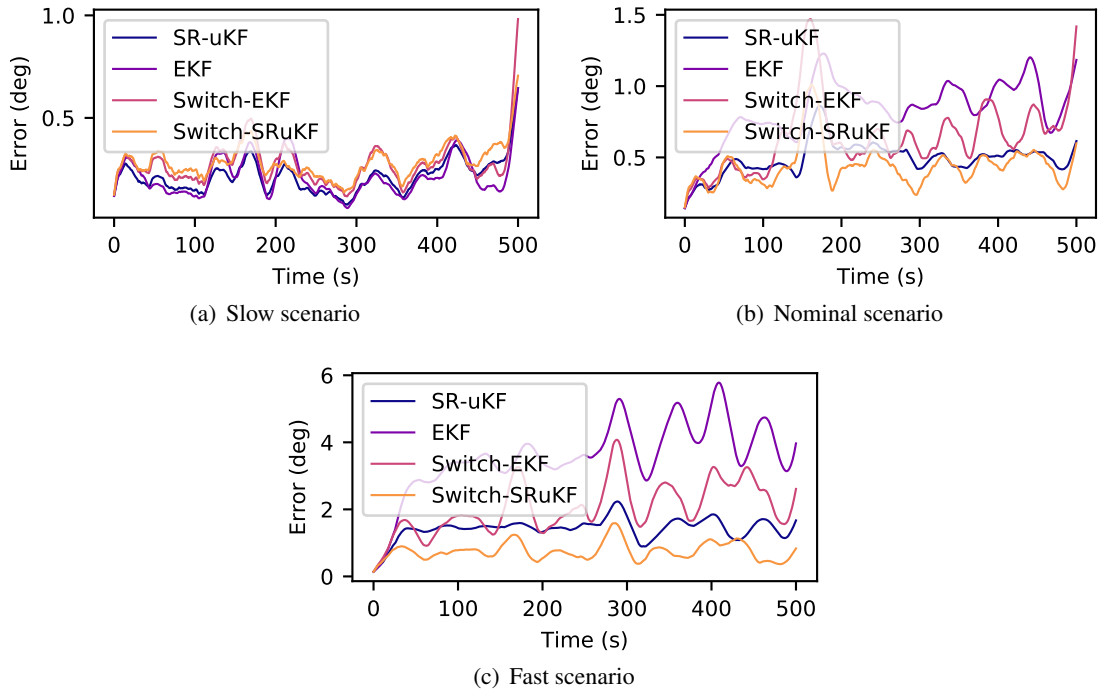


Figure 10. Average of 10 MC runs, FOV: 85°

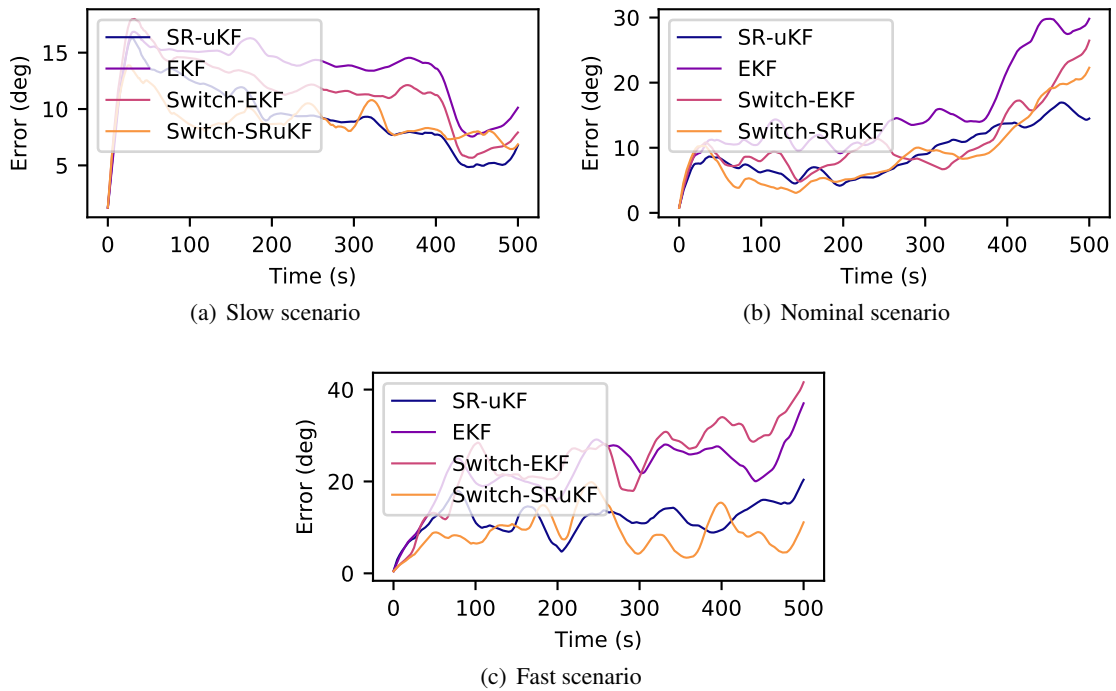


Figure 11. Average of 10 MC runs, FOV: 60°

CONCLUSIONS

This paper shows the comparative performances of several filters and formulations attempting to solve the CSS-only heading determination problem. In order to provide a better more robust algorithm, kinematics akin to MRPs shadow set switching are implemented. This leads to a change in the process noise derivation for an EKF, and requires a switch in the covariance on the rate states as well. At slow rates, all filters perform approximately the same. Then at higher rates, the switch formulations provide better results than all other filters implemented on the problem. Through these more complex kinematics, the Switch formulations analytically extract rate unobservability. This provides confidence in regard to the numerics of the filters as well as the overall state error.

More specifically, the Switch-SRuKF performs the best all around, whether the CSS have a narrow or wide field of view. The non-linear propagation of sigma points combined with the novel switch-formulation provides a good propagation step and allows for full utilization of the measurements despite inherent unobservability. In fact, Switch filters have removed the problem of the unobservable rate component from the estimation entirely. If combined with wide field-of-view CSS instruments it does not suffer from any observability issues, numerical or analytical.

REFERENCES

- [1] S. Allgeier, M. Mahin, and N. Fitz-Coy, *Design and Analysis of a Coarse Sun Sensor for Pico-Satellites*. American Institute of Aeronautics and Astronautics, 2017/12/19 2009, doi:10.2514/6.2009-1837.
- [2] W.-T. C. T. C. Fu-Yuen Hsiao and C. Rebelo, *Coarse Sun Acquisition Only with Sun Sensors for Micro Satellites*. AAS 15-319, 2015.
- [3] S. S. M. Swei, J. C. Fusco, and R. H. Nakamura, "Design of Sun-Safe Controllers for Lunar Atmosphere and Dust Environment Explorer," *Journal of Guidance, Control, and Dynamics*, Vol. 39, 2017/12/19 2016, pp. 2022–2033, 10.2514/1.G000270.
- [4] F. L. Markley and Y. Cheng, "Wahba's Problem with One Dominant Observation," *Journal of Guidance, Control, and Dynamics*, Vol. 41, Oct 2018.
- [5] J. Fusco, S. S.-M. Swei, and R. Nakamura, *Sun Safe Mode Controller Design for LADEE*. American Institute of Aeronautics and Astronautics, 2017/12/19 2015, doi:10.2514/6.2015-2011.
- [6] R. L. HUSTON, "Twin-gyro attitude control systems.," *Journal of Spacecraft and Rockets*, Vol. 3, 2019/01/29 1966, pp. 1136–1138, 10.2514/3.28613.
- [7] B. Chheda, A. Crassidis, and W. Walter, *Attitude Estimation Using an Accelerometer and Rate Gyro Based Device*. American Institute of Aeronautics and Astronautics, 2019/01/29 2006, doi:10.2514/6.2006-6279.
- [8] W. G. Breckenridge and A. J. Treder, "In-Flight Gyro Drift Rate Calibration on the Viking Orbiters," *Journal of Guidance, Control, and Dynamics*, Vol. 1, 2019/01/29 1978, pp. 433–439, 10.2514/3.55806.
- [9] C. J. Gioia and J. A. Christian, "Gyro Bias Estimation Using Interior Star Angles for Manual Attitude Determination," *Journal of Spacecraft and Rockets*, Vol. 54, 2019/01/29 2016, pp. 513–522, 10.2514/1.A33672.
- [10] D. Thakur and M. R. Akella, "Gyro-Free Rigid-Body Attitude Stabilization Using only Vector Measurements," *Journal of Guidance, Control, and Dynamics*, Vol. 38, April 2015.
- [11] S. Yang, M. R. Akella, and F. Mazenc, "Immersion and Invariance Observers for Gyro-Free Attitude Control Systems," *Journal of Guidance, Control, and Dynamics*, Vol. 39, November 2016.
- [12] H. Yoon and P. Tsiotras, "Spacecraft Angular Velocity and Line-of-Sight Control Using A Single-Gimbal Variable-Speed Control Moment Gyro," *AIAA Guidance, Navigation, and Control Conference and Exhibit*, No. 2005-6393, San Francisco, CA, AIAA, August 2005.
- [13] T. H. Mercker and M. R. Akella, "Rigid-Body Attitude Tracking with Vector Measurements and Unknown Gyro Bias," *Journal of Guidance, Control, and Dynamics*, Vol. 34, September-October 2011 2011.
- [14] T. Tsao and R. Chiang, *Gyroless Transfer Orbit Sun Acquisition Using Only Wing Current Feedback*. American Institute of Aeronautics and Astronautics, 2017/12/19 2009, doi:10.2514/6.2009-5944.
- [15] T. Iskenderian, "Lessons learned from selecting and testing spaceflight potentiometers," No. 19940028812, JPL, NASA. Lewis Research Center, The 28th Aerospace Mechanisms Symposium; p. p 339-358; NASA-CP-3260, 1994.

- [16] C. Anderson, "LEWIS spacecraft mission failure investigation board," final report, Air Force Research Laboratory, 1998.
- [17] T. Tsao and R. Y. Chiang, "Gyroless 3-Axis Sun Acquisition via Sun Sensors Only Unscented Kalman Filter Estimation," *AIAA Guidance, Navigation, and Control (GNC) Conference*, No. 2013-5025, Boston, MA, AIAA, August 2013.
- [18] S. A. O'Keefe and H. Schaub, "Gyro Accuracy and Failure Sensitivity of Underdetermined Coarse Sun Heading Estimation," *AAS/AIAA Space Flight Mechanics Meeting*, Williamsburg, VA, Jan. 11–15 2015. Paper AAS 15-344.
- [19] S. A. O'Keefe and H. Schaub, "Sun Heading Estimation using Underdetermined Set of Coarse Sun Sensors," *AAS/AIAA Astrodynamics Specialists Conference*, Hilton Head, SC, Aug. 11–15 2013. Paper No. AAS-13-891.
- [20] R. Y. Chiang and T. Tsao, *Gyroless 3-Axis Sun Acquisition via Sun Sensors Only Unscented Kalman Filter Estimation*. American Institute of Aeronautics and Astronautics, 2017/12/19 2013, doi:10.2514/6.2013-5025.
- [21] S. A. O'Keefe and H. Schaub, "On-Orbit Coarse Sun Sensor Calibration Sensitivity to Sensor and Model Error," *AAS/AIAA Space Flight Mechanics Meeting*, Williamsburg, VA, Jan. 11–15 2015. Paper AAS 15-392.
- [22] B. S. B. Tapley and G. Born, *Statistical Orbit Determination*. No. ISBN 9780126836301, Elsevier Academic Press, 2004.
- [23] H. Schaub and J. L. Junkins, *Analytical Mechanics of Space Systems*. Reston, VA: AIAA Education Series, 4th ed., 2018, 10.2514/4.105210.
- [24] T. Teil, H. Schaub, and S. Piggott, "Comparing Coarse Sun Sensor Based Sequential sun heading Filters," *AAS Guidance and Control Conference*, Breckenridge, CO, Feb. 1–7 2018. Paper AAS 18-011.
- [25] J. L. Crassidis and F. L. Markley, "Unscented Filtering for Spacecraft Attitude Estimation," *Journal of Guidance, Control, and Dynamics*, Vol. 26, July-August 2016.
- [26] R. v. d. Merwe, "The Square-Root Unscented Kalman Filter for State and Parameter-Estimation," *Acoustics, Speech, and Signal Processing*, 2001.
- [27] M. D. Shuster and S. D. Oh, "Three-Axis Attitude Determination from Vector Observations," *AIAA Journal of Guidance, Control, and Dynamics*, Vol. 4, No. 1, 1981, pp. 70–77.
- [28] H. Schaub and J. L. Junkins, "Stereographic Orientation Parameters for Attitude Dynamics: A Generalization of the Rodrigues Parameters," *Journal of the Astronautical Sciences*, Vol. 44, No. 1, 1996, pp. 1–19.
- [29] J. Alcorn and H. Schaub, "Simulating Attitude Actuation Options Using the Basilisk Astrodynamics Software Architecture," *67th International Astronautical Congress*, Guadalajara, Mexico, Sept. 26–30 2016.
- [30] A. Savitzky and M. J. E. Golay, "Smoothing and Differentiation of Data by Simplified Least Squares Procedures," *Analytical Chemistry*, Vol. 36 (8), July 1964, pp. 1627–1639.